

Gross errors in upper-mantle discontinuity topography from underside reflection data

Filip Neele,^{1,*} Han de Regt¹ and John VanDecar²

¹Department of Theoretical Geophysics, Utrecht University, PO Box 80021, 3508 TA, Utrecht, the Netherlands

²Department of Terrestrial Magnetism, Carnegie Institution, Broad Branch Road NW, Washington DC 20015, USA

Accepted 1997 January 2. Received 1996 December 9; in original form 1996 February 16

SUMMARY

Current models of upper-mantle discontinuity topography derived from traveltime variations of long-period underside reflections (P_dP or S_dS waves) may contain gross errors due to the use of geometrical optics in relating observed traveltimes to depth variations of the discontinuity near the reflection point. The use of geometrical optics is not valid if variations in the depth of the discontinuities exist on a lateral scale smaller than the size of the Fresnel zone in the data. Geometrical optics does not take into account the large size and the complex structure of the traveltime surface of underside reflections and may introduce spurious structure when used in inversions. Examples of synthetic long-period P_dP waveforms for reflections near subducting lithosphere show that scattering from expected small-scale depth variations of the discontinuities inside slabs causes complex waveform variations. For a 15–20 s P_dP wave, these small-scale depth variations (with a scale-length of 4°) are smaller than the Fresnel zone (roughly 20°) but larger than the P_dP wavelength at 420 km depth (about 150–200 km). The synthetic waveforms are processed to obtain P_dP traveltimes, which are in turn converted to apparent discontinuity depth at the reflection point using geometrical optics. The apparent discontinuity-depth variations are not only of the same order of magnitude as those obtained from real data but also exhibit artefacts that closely resemble features observed in current models. It is shown that large-scale (wavelengths of the order of 1000 km) downwarping of the 670-km discontinuity near subduction zones derived from underside reflection data can be explained as the long-wavelength manifestation of a single, small-scale (wavelengths of several hundreds of kilometres) deflection of the discontinuity inside and near subducting slabs.

Key words: 410 discontinuity, 670 discontinuity, upper mantle.

INTRODUCTION

This paper addresses waveform variations induced by lateral heterogeneities with a scale-length comparable to or smaller than the size of the Fresnel zone, for the special case of an underside reflection on the upper-mantle discontinuities (P_dP or S_dS waves, where d indicates the depth of the discontinuity). Underside reflections from upper-mantle discontinuities appear in the seismogram as precursors to the phases PP or SS . At distances larger than about 110° these waves arrive relatively undisturbed by other phases and thus provide an excellent means of sampling the discontinuities. Detailed knowledge of the topography on upper-mantle discontinuities will provide

important constraints on possible modes of convection in the Earth (see e.g. Phipps-Morgan & Shearer 1993).

Underside reflections (hereafter referred to as P_dP , but also including S_dS waves) are rarely positively identified on individual records. The PP -precursory signal shows a high degree of instability, even for closely spaced bounce points (see e.g. Bolt 1970; King, Haddon & Husebye 1975; Neele & Snieder 1992). Only stacking of a considerable number of records brings out evidence for the existence of P_dP arrivals (Wajeman 1988; Shearer 1990, 1991; Estabrook & Kind 1996). King *et al.* (1975) proposed a scattering mechanism as an explanation for the evasive nature of P_dP waves. In their model, the scattering occurs near the triplication distance, where amplitudes are high. Another explanation could be that the depth of the reflecting discontinuities varies laterally, causing traveltime variations of P_dP waves. Recently, Shearer (1991, 1993) and Shearer & Masters (1992) presented maps of

* Now at: TNO Physics and Electronics Laboratory, PO Box 96864, 2509 JG The Hague, the Netherlands.

depth variations of the 420- and 670-km discontinuities, obtained from traveltime variations of long-period $S_{420}S$ and $S_{670}S$ waves, using geometrical optics to convert traveltimes to discontinuity depth near the reflection point. Their models contain peak-to-peak depth variations of up to 30 km, with scale-lengths of several thousands of kilometres. However, the forward modelling results of Neele & Snieder (1992) show that the relation between depth variations of the reflector and the waveform of the P_dP or S_dS wave is not trivial. This is due to the saddle-shaped traveltime surface near the reflection point, which allows diffractions from scatterers far from the bounce point to arrive at nearly the same time as the arrival travelling along the geometrical ray path. The results of Neele & Snieder (1992) show that discontinuity depth variations on a scale smaller than the size of the Fresnel zone may have a significant effect on the waveform. Whereas these authors considered only amplitude variations, this paper addresses P_dP traveltime perturbations attributable to variations in the depth of the discontinuity near the bounce point of the P_dP wave. The results suggest that small-scale depth variations may cause serious artefacts when geometrical optics is used to interpret P_dP traveltime data in terms of discontinuity-depth variations near the reflection point. Conversely, undulations of the discontinuity that are significantly larger than the Fresnel zone (about 2000 km for 15–20 s P wave) are retrieved reasonably well using geometrical optics.

FORWARD MODELLING

Synthetic waveforms are calculated with the Kirchhoff-Helmholtz method of Frazer & Sen (1985) and Frazer (1987). This method builds the waveform at a given station through an integration over the reflecting discontinuity, summing all possible ray paths between the source, the discontinuity and the receiver. Geometrical spreading and phase delay are accounted for along each ray segment. A generalized reflection coefficient, assuming locally plane wavefronts, couples incoming and outgoing ray segments upon reflection on the discontinuity. The method allows a full 3-D treatment of the wave propagation effects. The reader is referred to Neele & Snieder (1992) for details about the computation of the synthetics for the present case of $P_{420}P$ and $P_{670}P$ waves.

Fig. 1(a) shows the $P_{420}P$ traveltime function in a spherically symmetric earth as a function of the position of the bounce point on the 420-km discontinuity; the epicentral distance is 110° . The source is at the surface, hence the point of stationary traveltime is at the mid-point between source and station. The PEMc model (Dziewonski, Hales & Lapwood 1975) is used as a reference model for all results presented in this paper. The (first) Fresnel zone is defined here as the collection of ray paths for which the traveltime difference with the geometrical ray path (i.e., the ray path that satisfies Snell's law) is no more than a quarter of the period. For periods of 15–20 s, the dominant frequency range of the long-period synthetics calculated below, the size of the Fresnel zone for an epicentral distance of 110° is about $15^\circ \times 15^\circ$ and has four tails extending to large distances. At 170° epicentral distance, the Fresnel zone measures about $15^\circ \times 50^\circ$, with its greatest length perpendicular to the source–receiver great circle. The long tails illustrate the minimax nature of all P_dP waves, resulting in a saddle shape of the traveltime function near the geometrical ray path. If topography exists on the discontinuity, the point

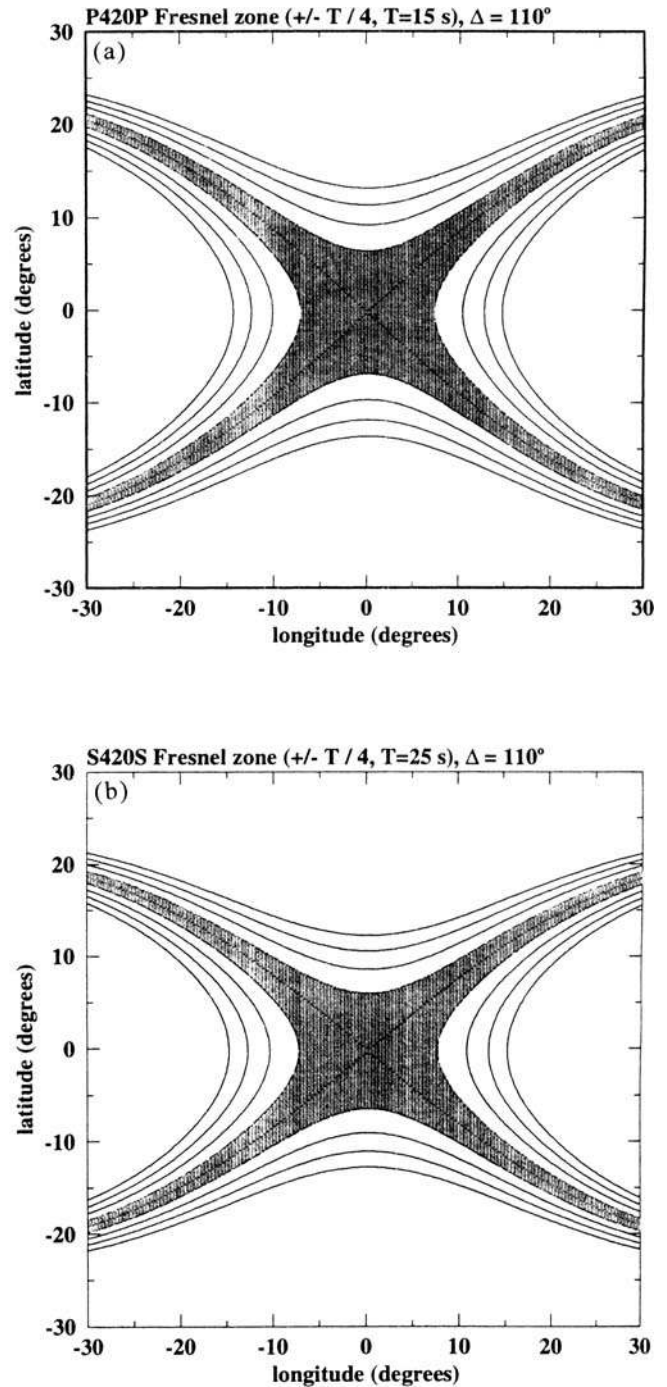


Figure 1. Traveltime surface for an underside reflection on the 420-km discontinuity. The source is at (lon, lat) = $(-55^\circ, 0^\circ)$, the receiver at $(55^\circ, 0^\circ)$. The shaded area is the first Fresnel zone (quarter-period). (a) $P_{420}P$ wave with a period of 15 s; (b) $S_{420}S$ wave with a period of 25 s.

of stationarity will move [and Fig. 1(a) suggests that it can easily move over large distances without changing the traveltime] and there may well be multiple stationary points, causing multi-pathing. If the scattering occurs along the source–receiver great circle, the energy will arrive ahead of the reference waveform. Diffractions from scatterers far from the geometrical bounce point (and off the great circle) may arrive at the same time as the ray-geometrical arrival and thus

affect its waveform, although the signal from within the tails has a low amplitude. The large size of the Fresnel zone allows many secondary stationary points to develop, and, if the appropriate discontinuity topography is present, the arrivals associated with these stationary points can have large amplitudes.

A simple subduction-zone model

Small-scale variations in the depth of the upper-mantle discontinuities are expected to occur where subducting slabs interfere with the 420- and 670-km discontinuities. Fig. 2 shows a simplified model of the depth variations expected for the 420-km discontinuity. As the olivine to β -spinel phase transition associated with the velocity jump at that depth is exothermic, the transition migrates to shallower depth in the cold slab. The slab in Fig. 2 is 40° long and its thermal signature is modelled by a cosine-square function 4° wide (see e.g. Helffrich, Stein & Wood 1989). Note that the width of the slab is much smaller than the size of the Fresnel zone for a period of 15 s, but larger than the spatial wavelength of a 15–20 s wave, which is about 150 km at 420 km depth. Assuming a Clausius–Clapeyron slope of 3.6 MPa K^{-1} (Liu *et al.* 1991) and a maximum temperature difference between the slab and the surrounding mantle of 500 K (Helffrich *et al.* 1989), the maximum elevation of the 420-km discontinuity is 50 km. The model used below for slab-induced topography of the 670-km discontinuity is the same as that in Fig. 2, except that the discontinuity inside the slab is depressed by 50 km, as the endothermic phase transition of β -spinel to perovskite plus magnesio-wüstite moves to greater depths inside a relatively cool slab. This is a reasonable model of topography of this discontinuity near and inside a subducting slab (Ito & Takahashi 1989). The reference model PEMc has an 8 per cent velocity jump at 670 km depth.

Synthetic $P_{420}P$ and $P_{670}P$ waveforms are calculated for source–station combinations with mid-points on a grid of $2^\circ \times 2^\circ$, covering the area of Fig. 2. For each synthetic, the source–receiver distance is 110° and the great circle through source and receiver is parallel to the longitude axis in Fig. 2. Figs 3(a) and (b) show the waveforms for the mid-points indicated by solid dots in Fig. 2, as a function of the distance from the centre of the subducting slab. A surface source is used for all calculations below.

The multichannel cross-correlation method developed by VanDecar & Crosson (1990) is used to obtain relative traveltime differences among the synthetics. The method calculates

the cross-correlation between all possible pairs of traces, and computes the relative lags that optimize the correlation in a least-squares sense. If there are multiple P_dP arrivals in a single synthetic, the time of the arrival with the best correlation is picked as the traveltime for that seismogram. Arrival times thus obtained are marked by a short dash in each trace in Figs 3(a) and (b).

The most striking feature in Figs 3(a) and (b) is a diffraction from the discontinuity perturbation near and inside the slab. This diffraction is most pronounced for the depressed 670-km discontinuity, illustrating the fact that a downwarping of the discontinuity generates more efficient focusing of P_dP energy than an upward deflection (see also Davis, Kind & Sacks 1989). The synthetics for mid-points about 8° away from the centre of the slab illustrate the sensitivity of P_dP waves for off-path structure. The interference between the diffraction from the slab and the ‘unperturbed’ P_dP arrival leads to late arrivals. The observed P_dP traveltimes cannot therefore, be directly interpreted in terms of the depth of the discontinuity at the mid-point. Early P_dP waves are observed for mid-points close to the slab, for both the $P_{420}P$ and $P_{670}P$ waves. Geometrical optics predicts non-zero traveltime perturbations only for mid-points within 2° of the slab centre, with a maximum of $+8$ s for $P_{420}P$ and -6 s for $P_{670}P$ waves.

Figs 4(a) and (b) show the traveltime variations observed for the model in Fig. 2, plotted as a function of the mid-point location. Traveltime differences are defined as the time obtained from the multichannel cross-correlation (for the slab model) minus the traveltime for the reference (flat discontinuity) model. Fig. 4(a) shows the results from $P_{420}P$ waves; results from $P_{670}P$ waves are given in Fig. 4(b). Although the traveltime variations are rather small (about 1 s) compared with the dominant period of the waveforms (about 15 s), these figures show two important results. First, the pattern of traveltime variations is complex: for both cases, there are early arrivals for mid-points near the centre of the slab and regions of late arrivals for mid-points at about 8° distance from the slab. The early arrivals for mid-points near the centre of the structure are unexpected for $P_{420}P$ waves, as geometrical optics predicts late arrivals there. Second, the results in Fig. 4(a) indicate that, depending on the location of the mid-point, both positive and negative traveltime perturbations with respect to a laterally homogeneous earth can be obtained. Using geometrical optics to relate P_dP traveltime perturbations to apparent discontinuity depth at the mid-point, the signal from a single elevation or depression could easily be interpreted in terms of a complex structure of the discontinuity, with peak-to-peak depth variations of about 12 km.

The similarity of Figs 4(a) and (b) indicates that P_dP traveltime data cannot differentiate between small-scale up- or downwarping of the discontinuity. Cross-sections of the traveltime along lines of zero latitude through the results in Figs 4(a) and (b) are shown in Fig. 5. The traveltimes have been converted to apparent depth of the discontinuity at the mid-point, using ray theory to compute the local derivative of the traveltime for the discontinuity depth. The figure indicates that, for the configuration of source used here, P_dP (or S_dS) data cannot differentiate between small-scale up- or downwarping of the discontinuity. The physical reason for this is that energy reflected by the slab-induced structure is weak, and that for mid-points close to the slab the P_dP wave is dominated by diffractions from the edges of the elevation or

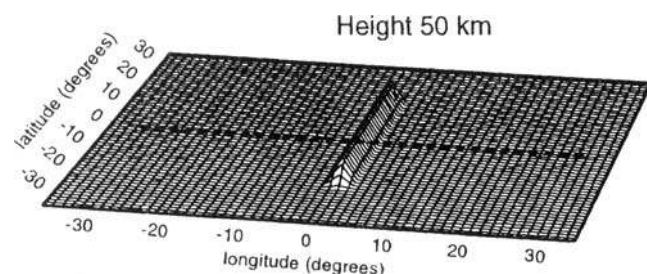


Figure 2. Simple model of slab-induced topography on the 420-km discontinuity. The elevation is modelled as a cosine-squared function of width 4° and height 50 km. Solid dots indicate the positions of the P_dP mid-points for the synthetics in Figs 3(a) and (b).

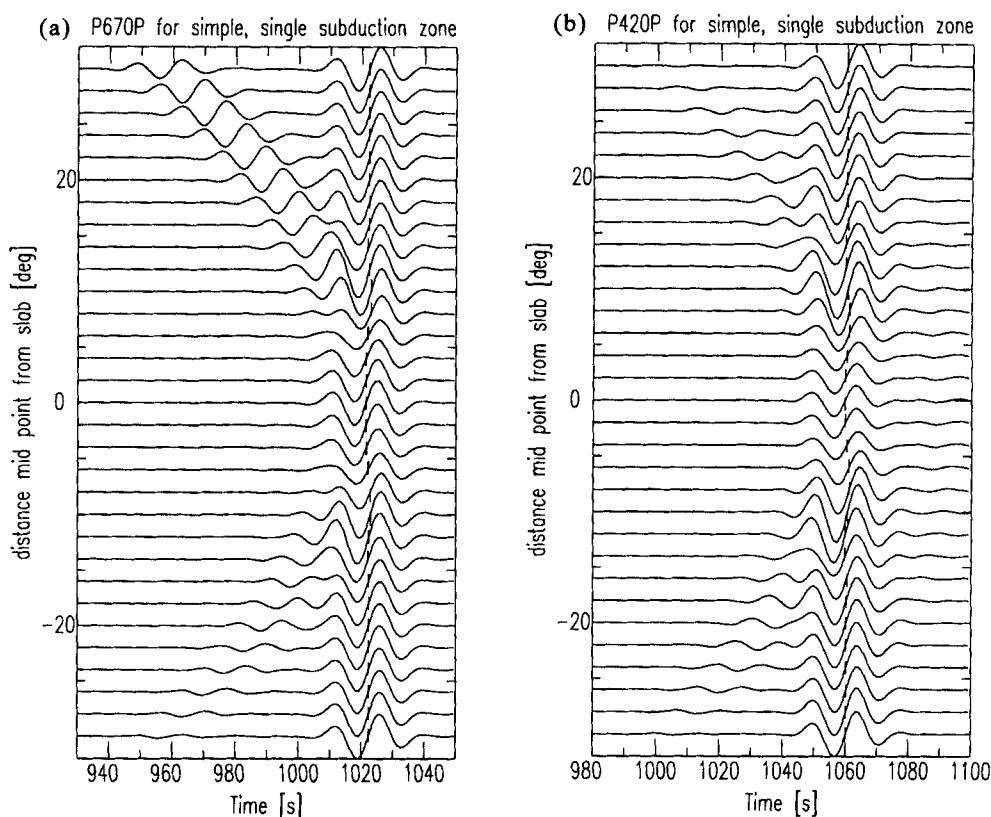


Figure 3. (a) Synthetic $P_{420}P$ waves for the model and mid-points in Fig. 2. A short dash indicates the traveltime found with multichannel cross-correlation. (b) As (a), for $P_{670}P$ waves. The source–receiver distance is 110° for all waveforms.

downwarping of the discontinuity, in the configuration used in Figs 3 to 5. These diffractions arrive relatively early as the diffraction takes place on the source–receiver great circle. Therefore, instead of the expected 8 s late ($P_{420}P$) or 6 s early ($P_{670}P$) wave, arrivals about 1 s early are observed.

Complex subduction-zone model and realistic data set

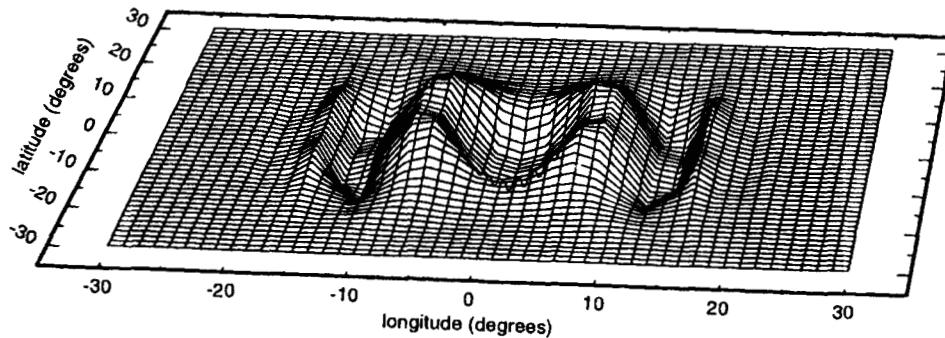
The results in Figs 3 to 5 were obtained for a data set with all great circles intersecting a simple discontinuity structure at the same azimuth with the epicentral distance fixed at 110° . The results of Neele & Snieder (1992) show that P_dP waveform perturbations strongly depend on the azimuth of the great circle, relative to the subducting slab. In a realistic data set with a more homogeneous azimuth and epicentral distance coverage, this may average out the effects of small-scale structure. We have used the event-station distribution of the data set used by Shearer (1993) and selected all event-station combinations with the mid-point in the north-west Pacific, as this is the region with the densest coverage of P_dP reflections. Mid-point locations are shown in Fig. 6; a short dash through each mid-point indicates the orientation of the great circle. The model of subduction zones developed by Snieder, Beckers & Neele (1991) is used for slab-induced discontinuity depth variations, assuming vertically descending slabs. The shaded regions in Figs 7–9 give the position and width of these discontinuity-depth perturbations. In the shaded regions, the depth perturbation is modelled as for the model of the single subduction zone in Fig. 2. Synthetic $P_{420}P$ and $P_{670}P$ waveforms were generated and cross-correlated to find relative

traveltime perturbations. These were converted to apparent discontinuity depths at the mid-point using ray theory.

Apparent depths thus obtained for the 420-km and 670-km discontinuities are presented in Figs 7(a) and (b), respectively. The depth variations depend strongly on both the position of the mid-point and the local azimuth of the great circle at the mid-point, as can be observed from several clusters and mid-points. The cluster near $25\text{--}30^\circ\text{N}$, 120°E , with great circles roughly perpendicular to the subduction zones, exhibits the same apparent depth variations as observed in Figs 4(a) and (b): increased discontinuity depths near the slab and shallower depths at about $7\text{--}10^\circ$ away from the slab. In general, the largest apparent depth perturbations are obtained for mid-points in the vicinity of the subduction zones, but the sign of the perturbations may be reversed, repeating the results of Fig. 4(a). For example, in Fig. 7(a) mid-points near 175°W , 50°N $P_{420}P$ yield traveltimes that suggest a downwarped 420-km discontinuity. The amplitude of the apparent depth variations is of the same order of magnitude as those observed in real S_dS data. Shearer's (1993) model of global 420- and 670-km discontinuity topography contains undulations of up to 20–30 km peak-to-peak amplitude, which is only two times the variations found here. Figs 7(a) and (b) show that in general the correct sign for the topography of the 670-km discontinuity is found, but that for the 420-km discontinuity apparent depths are more scattered. The reason for this is that downwarping of the discontinuity (at 670 km depth) leads to more efficient focusing of P_dP energy at the receiver, compared to an upward deflection of the boundary at 420 km depth (see

(a) 420-km discontinuity apparent depth

$$-6.6 \leq \Delta h \leq 4.1 \text{ km}$$

**(b) 670-km discontinuity apparent depth**

$$-5.4 \leq \Delta h \leq 8.5 \text{ km}$$

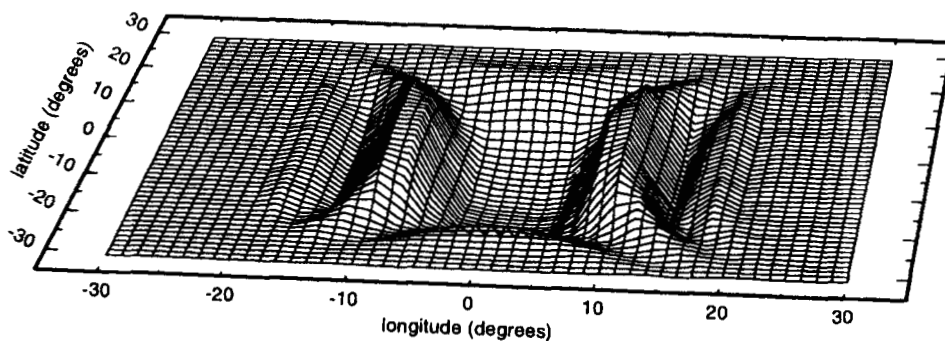


Figure 4. (a) $P_{420}P$ traveltime variations for the model in Fig. 2 displayed as a function of mid-point position. Traveltime perturbations vary from -0.7 to 1.1 s, corresponding to apparent discontinuity deflections between -6.6 and 4.1 km. Note that the model in Fig. 2 is a single elevation of 50 km height. (b) As (a), for $P_{670}P$ waves, and the model as in Fig. 2, but with an amplitude of -50 km. Apparent depths range from -5.4 to 8.5 km.

also Davis *et al.* 1989). Hence, the downwarped discontinuity is more easily observed in underside reflection data.

Figs 8(a) and (b) show apparent discontinuity depths as a function of the shortest distance between the mid-point and the slab. Mid-points on the Eurasian side of the subduction zones are plotted at negative distances. The solid line is the true discontinuity deflection. Also shown as solid dots are 4° averages and standard deviations, computed at 2° intervals; consecutive averages have half their data in common. The results for the two discontinuities are comparable to those in Fig. 5. The maximum apparent deflection of the discontinuity is about 10 km, and (low amplitude) upward deflections are seen at about 10° from the slab. Figs 8(a) and (b) illustrate that combining the data from a range of epicentral distances and azimuths does not reduce the signal from small-scale structure. It should be noted here that in the comparable figures of Shearer (1991) the slab deflection appears to be shifted to the back-arc side of the subduction zone. Although a true long-wavelength depression of the 670 -km discontinuity

may be present beneath the north-west Pacific, his results are expected to contain the same artefacts as those found here. Furthermore, the depression found in Shearer's results has the same amplitude and lateral extent as those found here and should therefore be interpreted with caution.

This is further emphasized in Figs 9(a) and (b), where the apparent depths for the 420 - and 670 -km discontinuities are averaged over partially overlapping circular caps of 10° radius, as done by Shearer (1993). To approximate the data processing of Shearer (1993), who measured the peak of a histogram of discontinuity-depth estimates, the mode, rather than the average, of the distribution of apparent discontinuity depths inside each cap is shown at the centre of the cap. Rather than reducing the signal from the small-scale, slab-induced discontinuity downwarping, the cap binning produces long-wavelength topography on the discontinuity, with peak-to-peak amplitudes of about 10 km in both cases.

The apparent depth variations found in Figs 7(a) and (b) range between about -15 and $+15$ km, with outliers at over

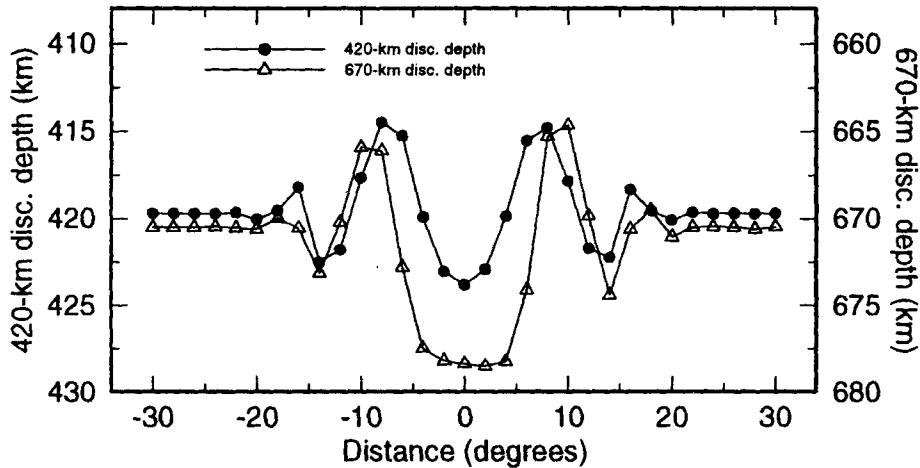


Figure 5. Cross-sections taken perpendicular to, and across the centre of, the synthetic slab anomaly (as shown by the dashed line in Fig. 2). Distance is the distance of the bounce point from the centre of the slab-induced discontinuity topography. Again, the true topography has a width of 4° and a height (for the 420-km discontinuity) or depth (for the 670-km discontinuity) of 50 km.

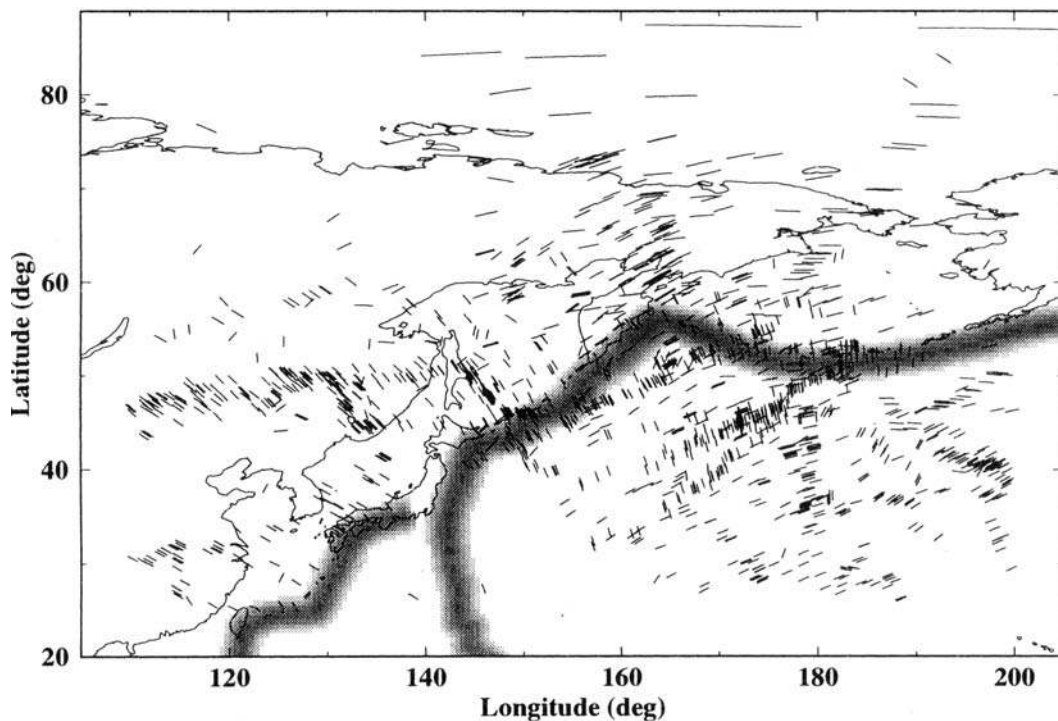


Figure 6. Distribution of P_4P mid-point locations in the north-west Pacific as used by Shearer (1993). The short dash indicates the orientation of the source-receiver great circle at the mid-point. The shaded region (width 4°) indicates the position of the subducting slabs used in the calculations of synthetic P_4P waveforms. In the shaded region, the depth perturbation of the discontinuity varies as described in the caption of Fig. 2.

100 km. It is of course not valid to use the local derivative of traveltime to discontinuity depth at the mid-point to relate P_4P traveltimes to such large depth perturbations. The actual value of these outliers is therefore not important. They do, however, indicate that if a diffraction from structure off the great circle is sufficiently strong, it may be interpreted as the underside reflection from a discontinuity at a possibly very different depth (see also Shearer 1993, Fig. 24). A result of the large size of the Fresnel zone, this presents a major problem in interpreting P_4P or S_4S waveforms in terms of discontinuity structure.

As a final example, $P_{420}P$ waveforms are calculated for the mid-point locations in Fig. 6 and a model of long-wavelength undulations of the 420-km discontinuity. The undulations were modelled as an egg-box function, given by $A \cos(k\phi) \cos(k\psi)$, where ϕ is longitude, ψ is latitude and k the wavelength in both longitude and latitude ($k = 60^\circ$). The amplitude A of the undulations is 20 km. The true model is indicated in Fig. 10(a), where circles and crosses represent up- and downwarping of the discontinuity, respectively. Fig. 10(b) shows the apparent depths again obtained using geometrical optics. Both position and amplitude of these long-wavelength undulations are

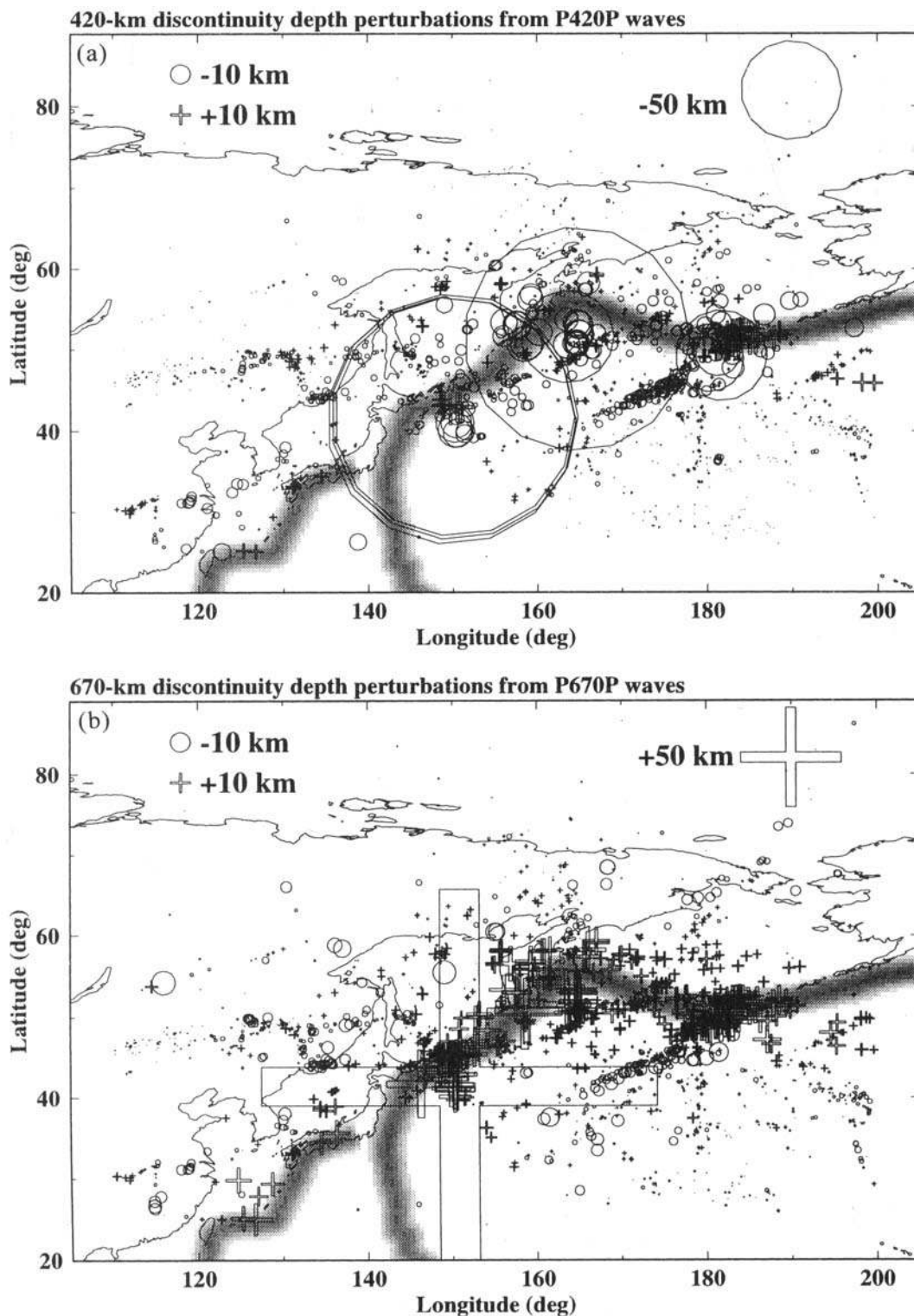


Figure 7. Apparent 420-km discontinuity depths obtained for the model of subduction zones. Crosses represent a locally deeper, circles a locally shallower, discontinuity. At the upper right of the figures the symbol size for the depth perturbation corresponding to the true topography is given. Note that significant apparent discontinuity-depth perturbations are found for bounce-point locations far from the subducting slabs, and that these perturbations may vary strongly between closely spaced bounce points. (a) 420-km discontinuity; (b) 670-km discontinuity.

retrieved well by the long-period $P_{420}P$ waves, and the use of geometrical optics in relating traveltime to discontinuity depth is in general justified. Some exceptions to the rule are seen near 125°E, 45°N, where a very large apparent upwarping is

observed in the data. This is due to signal from structure off the great circle that dominates the waveform. This signal arrives late, and hence is interpreted as a large local depth perturbation.

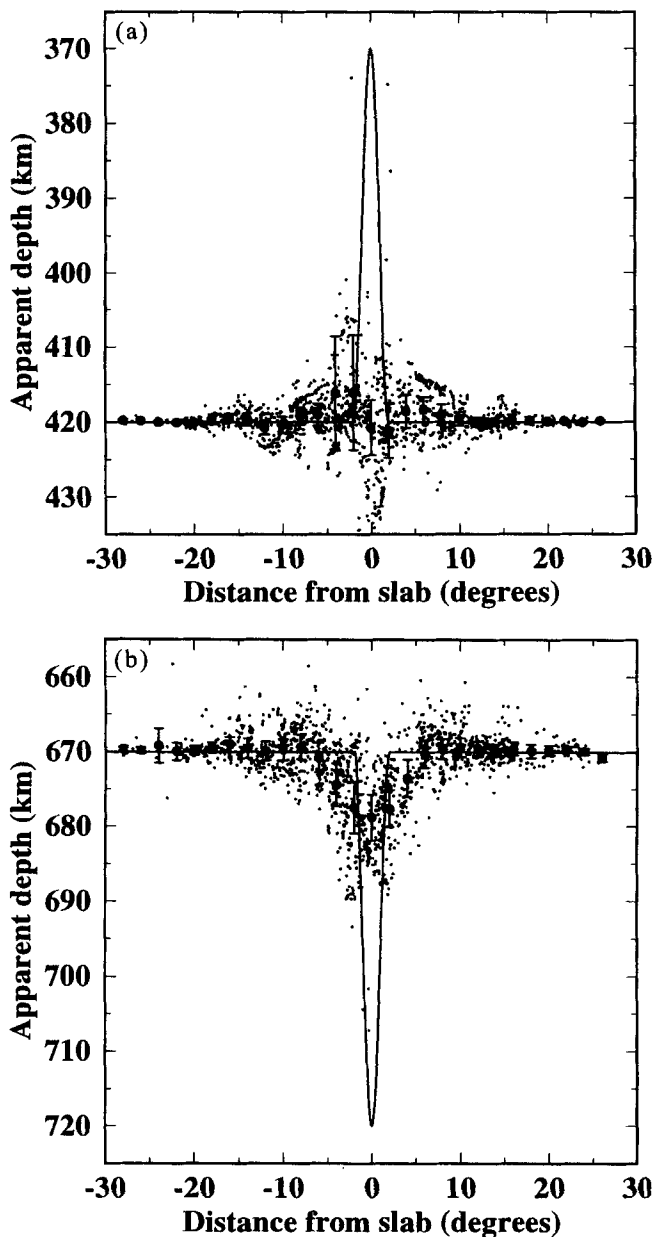


Figure 8. Apparent discontinuity depths as a function of the distance of each mid-point in Fig. 7 to the nearest subduction zone. The solid line indicates the true depth variations. Averages over 4° intervals are given by the solid dot, plotted at the centre of each interval; one standard deviation error bars are also shown. (a) 420-km discontinuity; (b) 670-km discontinuity.

DISCUSSION

The results presented here show that simple small-scale (as compared to the size of the Fresnel zone) discontinuity-depth variations cause strong P_dP waveform perturbations. The slab-induced depth variations used here, although smaller than the Fresnel zone of a long-period P_dP wave, are larger than the wavelength of a 15–20 s underside reflection at 420 km depth, and are, therefore, not averaged out by the P_dP wave. Apparent discontinuity-depth variations are obtained from the synthetic waveforms by converting traveltime perturbations to discontinuity-depth perturbations. Geometrical optics is used

to compute the local derivative of traveltime to discontinuity depth at the P_dP reflection point. This procedure does not take into account the large size and complexity of the P_dP Fresnel zone. The saddle shape of the traveltime function near the mid-point allows energy scattered from structure far from the mid-point to arrive both earlier and later than the main arrival. Multiple stationary points may develop in the presence of topography on the discontinuity, and the P_dP energy may be distributed over multiple arrivals. A ray-geometrical approach is not adequate in such cases, as it does not take into account the effect of structure far from the mid-point; implicitly, a scattering effect is then interpreted using ray theory. Attributing the observed traveltime perturbation to a discontinuity-depth perturbation at the geometrical reflection point may cause both a large mislocation of diffractors and an incorrect discontinuity depth.

All computations presented above apply to the case of P_dP waves, yet the results are relevant to the case of S_dS reflections. These waves constitute the primary data set used in the construction of current maps of upper-mantle discontinuity topography (Shearer 1991, 1993; Shearer & Masters 1992), although Estabrook & Kind (1996) recently used P_dP waves to image the discontinuities. Fig. 1(b) shows the $S_{420}S$ Fresnel zone, for an epicentral distance of 110° and a period of 25 s, the dominant period in long-period WWSSN S -wave data. It is obvious that the Fresnel zones in Figs 1(a) and (b) have comparable size. Therefore, the effects of subduction zones on S_dS waveforms are comparable to those presented above for P_dP waves. Furthermore, non-planar discontinuities lead to coupling between the SH and SV wavefields. Such effects are not included here, and add further complexity to the relation between discontinuity structure and S_dS waveforms.

This has implications for current models of discontinuity topography derived from P_dP or S_dS data (Shearer 1991, 1993; Shearer & Masters 1992). Derived from S_dS traveltime using simple ray geometry, these models may be seriously affected by the mapping of small-scale, slab-induced discontinuity topography into long-wavelength discontinuity undulations. The pattern displayed in Figs 5, 8(a) and (b) (a central peak or trough with side lobes) strongly resembles that found by Shearer (1991) and Shearer & Masters (1992) from observed S_dS traveltimes as a function of the distance of the reflection point from a subducting slab. Furthermore, the magnitude of apparent depths in Figs 7 and 8 has the same order of magnitude as those found from real data. Another argument supporting the mapping of small scales into large scales ('spectral leakage') is that the downwarping of the 670-km discontinuity in Shearer's models occurs mainly near subduction zones around the Pacific. Therefore, in any study of true long-wavelength variations in the depth of the upper-mantle discontinuities using underside reflections, the effect of small-scale variations must be taken into account. Recently, Trampert & Snieder (1996) presented both a formal explanation of the occurrence of spectral leakage in tomographic inversions and a method to minimize such effects.

The synthetics shown in Fig. 3 contain diffractions from structure for the geometrical reflection point that may be strong and dominate the signal. These explain the very large apparent depth perturbations in Fig. 7. Such diffractions will interfere with underside reflections from discontinuities at different depths. Such interference effects will further complicate the interpretation of P_dP and S_dS data in terms of

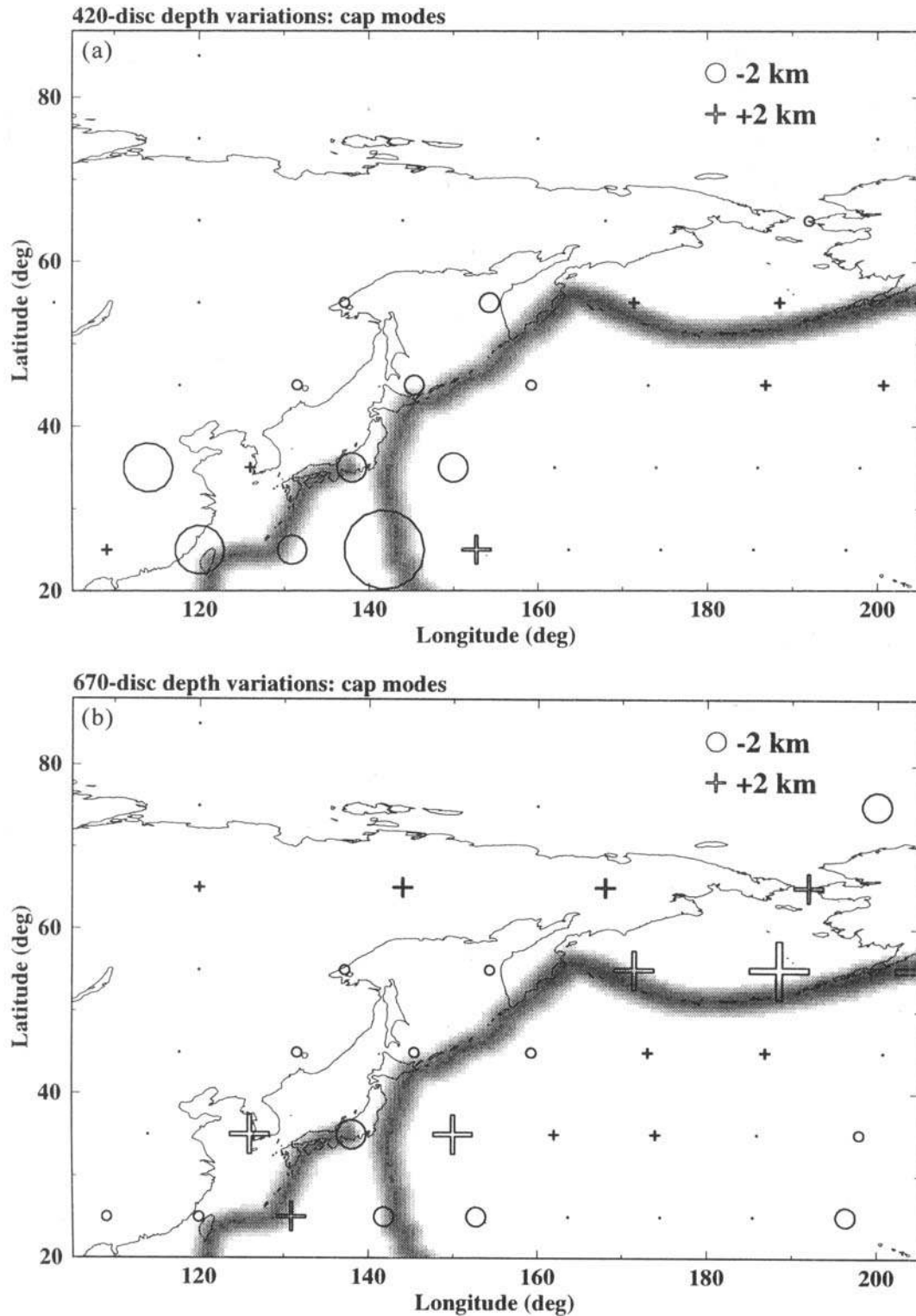


Figure 9. Apparent depth perturbations from Fig. 7 averaged over caps of radius 10° ; the mode of the perturbations in each cap is plotted at the cap centre. Note that the scale is different from that in Fig. 7. (a) 420-km discontinuity, cap modes range from -8 to $+4$ km; (b) 670-km discontinuity, modes range from -3 to $+6$ km.

discontinuity topography. The misidentification of such early- or late-arriving strong diffractions may also explain some of the discontinuities at depths other than around 420 or 670 km as reported by Shearer (1993).

Reliable estimates of discontinuity topography can only be obtained from P_dP or S_dS data if the inversion method accounts for the complex Fresnel zone structure of P_dP or S_dS waveforms. Such a method is currently being tested and will

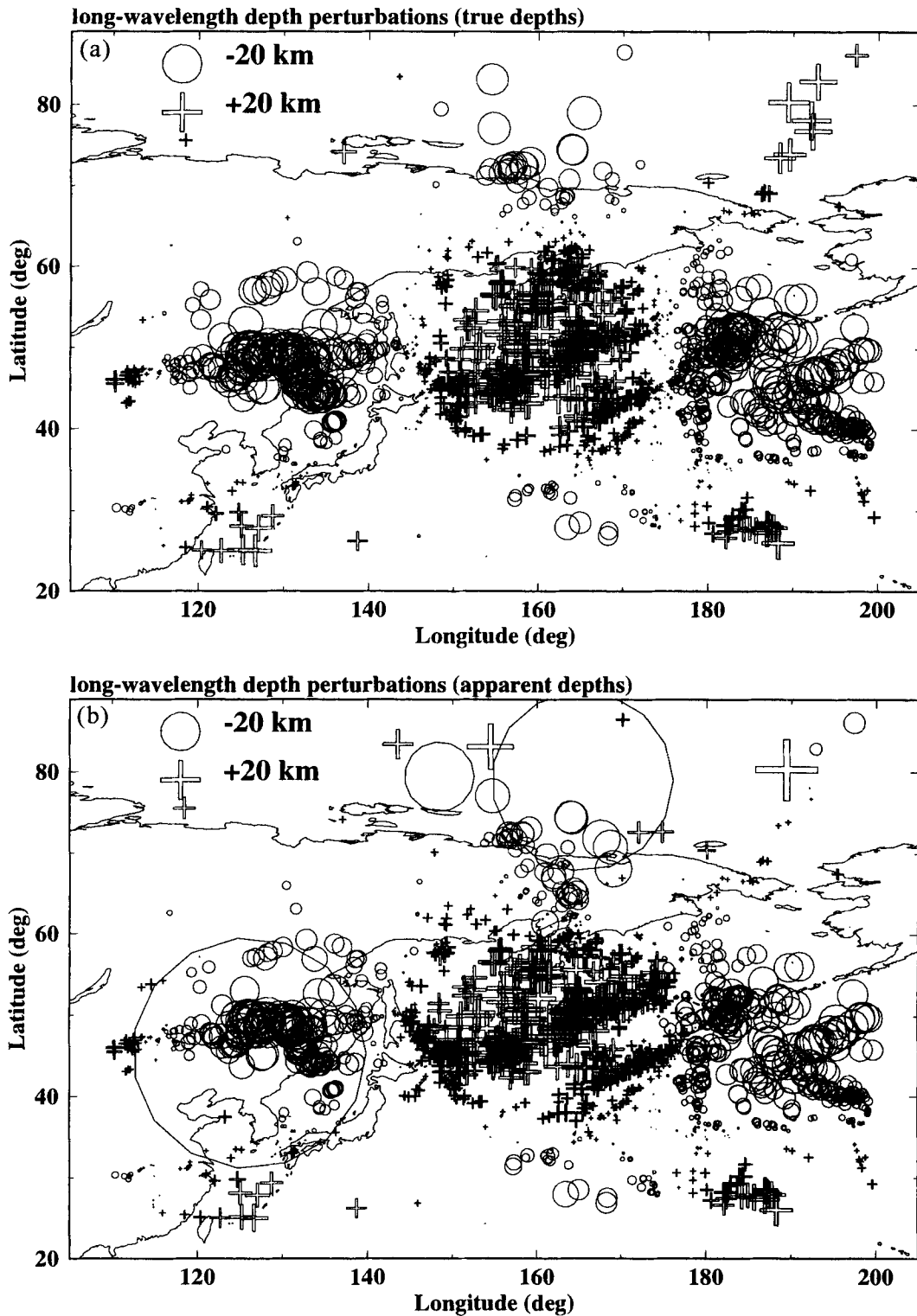


Figure 10. (a) True 420-km discontinuity depth perturbations for a long-wavelength egg-box model of discontinuity undulations, plotted at the bounce points of Fig. 6. The model has wavelengths of 60° in both latitude and longitude and an amplitude of 20 km. (b) Apparent discontinuity-depth variations obtained from $P_{420}P$ waves calculated for the egg-box model. There is good general agreement between Figs 10(a) and (b), indicating that structures with wavelengths larger than the size of the Fresnel zone (which is about 20° for 15 s waves) are retrieved well.

be presented in a future paper. It should be noted that in the computations presented here, noise or other mechanisms that may further affect the P_dP waveform (surface topography, volume heterogeneities) have not been taken into account.

Similar mechanisms, for example lateral variations in Moho depth or surface topography, may be the cause of observed PP and SS waveform variability (Paulssen & Stutzmann 1996).

ACKNOWLEDGMENTS

We thank Peter Shearer for providing us with his data set. Helpful discussions with Roel Snieder and Hanneke Paulssen are greatly appreciated; we thank Laura Jones for carefully reading the manuscript. Comments from Peter Shearer and Jürgen Neuberg are gratefully acknowledged. This research was supported by the Netherlands Organization for Scientific Research (NWO) through the Pioneer project PGS 76-144. This is Geodynamic Research Institute (Utrecht University) publication 96.038.

REFERENCES

- Bolt, B., 1970. P_4P and $PKiKP$ waves and diffracted PcP waves, *Geophys. J. R. astr. Soc.*, **20**, 367–382.
- Davis, J.P., Kind, R. & Sacks, I.S., 1989. Precursors to $P'P'$ re-examined using broad-band data, *Geophys. J. Int.*, **99**, 595–604.
- Dziewonski, A.M., Hales, A. & Lapwood, E., 1975. Parametrically simple Earth models consistent with geophysical data, *Phys. Earth planet. Inter.*, **10**, 12–48.
- Estabrook, C.H. & Kind, R., 1996. The nature of the 660-km upper mantle seismic discontinuity from precursors to PP, *Science*, **274**, 1179–1182.
- Frazer, L.N., 1987. Synthetic seismograms using multifold path integrals—I. Theory, *Geophys. J. R. astr. Soc.*, **88**, 621–646.
- Frazer, L.N. & Sen, M.K., 1985. Kirchhoff–Helmholtz reflection seismograms in a laterally inhomogeneous multi-layered elastic medium—I. Theory, *Geophys. J. R. astr. Soc.*, **80**, 121–147.
- Helffrich, G.R., Stein, S. & Wood, B.J., 1989. Subduction zone thermal structure and mineralogy and their relationship to seismic wave reflections and conversions at the slab/mantle interface, *J. geophys. Res.*, **94**, 753–763.
- Ito, E. & Takahashi, E., 1989. Postspinel transformations in the system Mg_2SiO_4 – Fe_2SiO_4 and some geophysical implications, *J. geophys. Res.*, **94**, 10 637–10 646.
- King, D.W., Haddon, R.A.W. & Husebye, E.S., 1975. Precursors to PP, *Phys. Earth planet. Inter.*, **10**, 103–127.
- Liu, M., Yuen, D.A., Zhao, W. & Honda, S., 1991. Diapiric instabilities in the upper mantle due to phase transitions, *Science*, **252**, 1836–1839.
- Neele, F. & Snieder, R., 1992. Topography of the 400-km discontinuity from observations of long-period $P400P$ phases, *Geophys. J. Int.*, **109**, 670–682.
- Paulssen, H. & Stutzmann, E., 1996. On PP–P differential traveltime measurements, *Geophys. Res. Lett.*, **23**, 1833–1836.
- Phipps-Morgan, J. & Shearer, P., 1993. Seismic constraints on mantle flow and topography of the 660-km discontinuity: evidence for whole-mantle convection, *Nature*, **365**, 506–511.
- Shearer, P.M., 1990. Seismic imaging of upper mantle structure—new evidence for a 520 km discontinuity, *Nature*, **344**, 121–126.
- Shearer, P.M., 1991. Constraints on upper mantle discontinuities from observations of long-period reflected and converted phases, *J. geophys. Res.*, **96**, 18 147–18 182.
- Shearer, P.M., 1993. Global mapping of upper mantle reflectors from long-period SS precursors, *Geophys. J. Int.*, **115**, 878–904.
- Shearer, P.M. & Masters, T.G., 1992. Global mapping of topography on the 660-km discontinuity, *Nature*, **355**, 791–796.
- Snieder, R., Beckers, J. & Neele, F., 1991. The effect of small-scale structure on normal mode frequencies, *J. geophys. Res.*, **96**, 501–515.
- Trampert, J. & Snieder, R., 1996. Model estimations based on truncated expansions: Possible artifacts in seismic tomography, *Science*, **271**, 1257–1261.
- VanDecar, J.C. & Crosson, R.S., 1990. Determination of teleseismic relative phase arrival times using multichannel cross-correlation and least squares, *Bull. seism. Soc. Am.*, **80**, 1049–1061.
- Wajeman, N., 1988. Detection of underside P reflections at mantle discontinuities by stacking broadband data, *Geophys. Res. Lett.*, **15**, 669–672.